Fused coarse-grained model of aromatic ionic liquids and their behaviour at electrodes.

Li, Bin; Ma, Ke; Wang, Yong-Lei; Turesson, Martin; Woodward, Clifford E; Forsman, Jan

Published in:
Physical chemistry chemical physics : PCCP

DOI:
10.1039/c6cp00202a

2016

Citation for published version (APA):
Li, B., Ma, K., Wang, Y.-L., Turesson, M., Woodward, C. E., & Forsman, J. (2016). Fused coarse-grained model of aromatic ionic liquids and their behaviour at electrodes. *Physical chemistry chemical physics : PCCP*, *18*(11), 8165-8173. https://doi.org/10.1039/c6cp00202a

Total number of authors:
6

Journal Name

ARTICLE TYPE

Cite this: DOI: 10.1039/xxxxxxxxxx

Fused coarse-grained model of aromatic ionic liquids and their behaviour at electrodes

Bin Li,*[a] Ke Ma,[b] Yong-Lei Wang,[c,d] Martin Turesson,[a] Clifford E. Woodward[b] and Jan Forsman*[a]

Received Date
Accepted Date

DOI: 10.1039/xxxxxxxxxx

www.rsc.org/journalname

A fused coarse-grained model of aromatic ionic liquids 1-alkyl-3-methylimidazoliums tetrafluoroborate ([C_nMIM$^+$][BF_4^-]) has been constructed. Structural and dynamical properties calculated from our model are compared with experimental data as well as with corresponding results from simulations of other suggested models. Specifically, we adopt a fused-sphere coarse-grained model for cations and anions. This model is utilized to study structure and differential capacitance in models of flat and porous carbon electrodes. We find that the capacitance varies with pore size, in a manner that is related to the packing of ions inside the pore. For very narrow pores, diffusion is slow and the establishment of thermodynamic equilibrium may exceed the practical limits for our Molecular Dynamics simulations.

1 Introduction

Room temperature ionic liquids (ILs) are salts that form a stable liquid at about room temperature. In recent years, ILs have attracted considerable attention, in terms of fundamental research as well as application-oriented work. This is at least partly motivated by their characteristic properties, such as a low melting point, a high viscosity, and negligible vapour pressure. Furthermore, many ILs have unique solvent properties, and some of them are even able to dissolve cellulose.[1–4] ILs are also viable candidates as electrolytes in electric double layer capacitors (EDLCs),[5–9] primarily due to their good electrochemical stability and short Debye screening lengths. Note also that neat ILs do not have a solvation shell, which further enhances their ability to screen charge. This screening can be quantified in terms of a potential drop across the electric double layer, formed at the electrode surface, so the structures near interfaces are highly relevant to the properties of the capacitors.

If ILs are combined with nanoporous electrodes, which have large effective surface area, one may obtain an enormous capacitance. Such devices are often called “supercapacitors”. The specific capacitance, as a function of applied voltage, is also denoted as differential capacitance, DC. Generally speaking, the DC drops at very high absolute values of applied voltage, as a result of saturation effects. However, in some cases, the DC also displays a local minimum for nearly neutral electrodes, resulting in a “camel-shaped” DC curve. This minimum may be related to surface depletion.[10–14] The DC can also be expected to depend upon the size of the nanopores. There is experimental evidence supporting this conjecture, but the results are still controversial.[15–20]

Due to the high viscosity of ILs, the simulation of a realistic model system will be time-consuming, with a high computational cost. Hence, simulations of coarse-grained (CG) IL models is an attractive alternative. A spherical CG bead usually represents a group of atoms or molecules. Some CG models of ILs are built via a systematic “bottom-up” procedure, such as multiscale coarse-graining (MS-CG) or the effective force coarse-graining (EF-CG) approaches by Wang *et al.*,[21–23] and other CG approaches include the Newton inversion (NI) iterative Boltzmann inversion (IBI) methods.[24] On the other hand, CG models have also been constructed by matching the structural and dynamical properties from experiments and all-atom simulations, via a “top-down” approach. Sun and Zhou developed a CG model of ILs with Nafion by using a Martini CG force field.[25] Roy and Maroncelli used a 4-site CG model to represent the ILs 1-butyl-3-methylimidazolium hexafluorophosphate ([Im_{41}^+][PF_6^-]),[26] and Merlet *et al.* developed a similar CG model for 1-alkyl-3-methylimidazoliums tetrafluoroborate ([C_nMIM$^+$][BF_4^-]).[27]

About five years ago, we constructed a simple CG model of imidazolium-based ILs, which had the advantage of being straightforwardly treated via classical density functional theory (DFT) methods.[14] The accuracy of the DFT treatment was evaluated by direct comparisons of structural properties and DC curves,

---

[a] *Theoretical Chemistry, Chemical Centre, Lund University, P.O. Box 124, S-221 00 Lund, Sweden; E-mail: jluchemlib@gmail.com, jan.forsman@teokem.lu.se*
[b] *School of Physical, Environmental and Mathematical Sciences, University College, University of New South Wales, ADFA, Canberra ACT 2600, Australia*
[c] *System and Component Design, Department of Machine Design, KTH Royal Institute of Technology, SE-100 44 Stockholm, Sweden*
[d] *Applied Physical Chemistry, Department of Chemistry, KTH Royal Institute of Technology, SE-100 44 Stockholm, Sweden*

determined with Metropolis Monte Carlo (MC) simulations.[12] Recently, we developed a more detailed CG model of imidazolium-based ILs. This is more complex than the original version, but still manageable by DFT approaches,[28] which offers substantial computational benefits. The model was evaluated via a combination of MC and molecular dynamics (MD) simulations. The CG model is indeed able to reproduce some structural properties, for example, bulk densities.

Although the CG model could reproduce structural properties, it unfortunately generates rather inaccurate dynamical properties. Specifically, simulated diffusion coefficients are considerably larger than corresponding experimental data. In this work, we make some modifications to the model, retaining the architectural structure, with the aim to improve the dynamical properties while keeping the high accuracy of bulk structural predictions.

The paper is organized as follows: in Sec. 2 we present details of our newly developed CG model for aromatic ILs, as well as our models for electrodes and some MD simulation details. Sec. 3 contains our validation of the CG model, while behaviours at electrodes are scrutinized in Sec. 4. Finally, in Sec. 5, we summarize the main conclusions of this work.

2 Model and methods

2.1 CG model

In the model presented here, the bond-lengths were generally smaller than the diameter of the spheres, resulting in our "fused bead" model. A simple cartoon of the CG model of $[C_4MIM^+][BF_4^-]$ is shown in Fig. 1, although we note that the bond lengths are exaggerated in the graph, as the beads are actually fused. For different 1-alkyl-3-methylimidazoliums cations, we just changed the alkyl chain length by adding or removing neutral beads (one bead per -CH_2- group). The non-bonded interactions between CG beads are modelled with Lennard-Jones (LJ) and Coulomb interactions,

$$U_{ij}(r_{ij}) = 4\varepsilon_{ij}\left[\left(\frac{\sigma_{ij}}{r_{ij}}\right)^{12} - \left(\frac{\sigma_{ij}}{r_{ij}}\right)^{6}\right] + \frac{z_i z_j e^2}{4\pi\varepsilon_0\varepsilon_r r_{ij}} \tag{1}$$

in which ε and σ are the well depth and the bead diameter, respectively, z is the valency of the charged CG bead, ε_0 is the vacuum permittivity and ε_r is the relative permittivity. The CG beads are connected via harmonic bonds,

$$V_{ij}(r_{ij}) = \frac{1}{2}k_b(r_{ij} - r_0)^2 \tag{2}$$

here k_b is the force constant of the harmonic bond and r_0 is the equilibrium length. In our previous model, all the CG beads had the same size ($\sigma = 0.24$ nm) and r_0 was set equal to σ. Furthermore, all beads in that model interacted with a common LJ strength ($\varepsilon = 100 k_B K$).[28] But as the dynamical properties of our previous model were not consistent with experimental results, we shall implement some adjustments to this model.

We have set $\sigma = 0.335$ nm and $r_0 = 0.17$ nm for all the beads in the fused model. The force constant of the harmonic bonds was set as relatively strong, 1×10^5 KJ·mol^{-1}·nm^{-2}. We utilized three types of CG beads to represents the IL pair. The CG beads which represent alkyl chain are neutral, and the CG beads in the two star-shape parts carry partial charges, $+0.2\ e$ in the cations and $-0.2\ e$ in the anions, representing the aromatic ring and $[BF_4^-]$, respectively. As in our previous model, the relative permittivity ε_r was set to 2.3, which is the value for benzene. The choice was motivated by the aromatic structure of the cations. In contrast to our previous model, we assume that the electronic polarizability of neutral beads is weaker than that of charged beads, as manifested by their LJ energy parameter. Specifically, ε_{cc} =1.7 KJ·mol^{-1}, and ε_{nn} = 0.3 KJ·mol^{-1}, with index "cc" and "nn" denoting "charged-charged" and "neutral-neutral", respectively. The intramolecular LJ interactions are excluded up to two neighbour CG beads, but the intramolecular Coulomb interactions between adjacent charged CG beads still exist in order to keep the charged parts of ILs as star architectures. The masses of neutral, positive and negative beads, were set to 14.4, 13.6 and 17.4 amu.

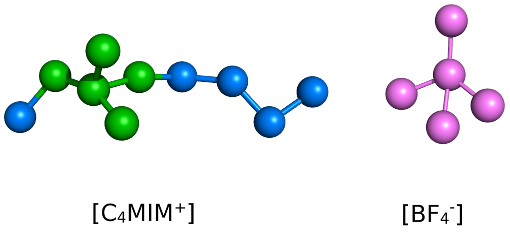

Fig. 1 CG model of IL $[C_4MIM^+][BF_4^-]$. The blue, green and pink CG beads represent particles without charges, with positive charges and negative charges, respectively. The bonds have been extended, for clarity. In reality, the beads overlap, forming a fused-sphere model.

2.2 Electrode description

We utilized an analogous 3-layer model in a flat geometry, designed to mimick a single non-porous electrode surface. In our model, two parallel 3-layer surfaces are separated by 15 nm (the "IL region" is between the inner layers), which is large enough for them to be regarded as two isolated surfaces. Periodic boundary conditions were applied in the x, y directions parallel with the surfaces, i.e., we attempted to model flat surfaces that are essentially infinite in these directions. The simulation box extended 6 nm× 6.3 nm, in the x and y directions. A snapshot of the system, including ILs and the flat model graphene electrodes, is illustrated in Fig. 2 (a). The fixed partial charges are distributed on the carbon atoms in the layers at the IL interface.

A 3-layer thick carbon nanotube (CNT) model was used to represent a cylindrical electrode pore, a geometrically more complex electrode. The cylinder symmetry axis is aligned with the z direction. A charged electrode was modelled by adding fixed partial charges on the carbon atoms on the inner layer of the CNT. The 3-layer architecture ensures that the interactions between the inner parts (the pore itself, and the inner surface) and the ILs near the outer surface, is weak. Ideally, this interaction would be completely negligible, given that our model is designed to mimick an electrode pore. The snapshot of a system containing the pore,

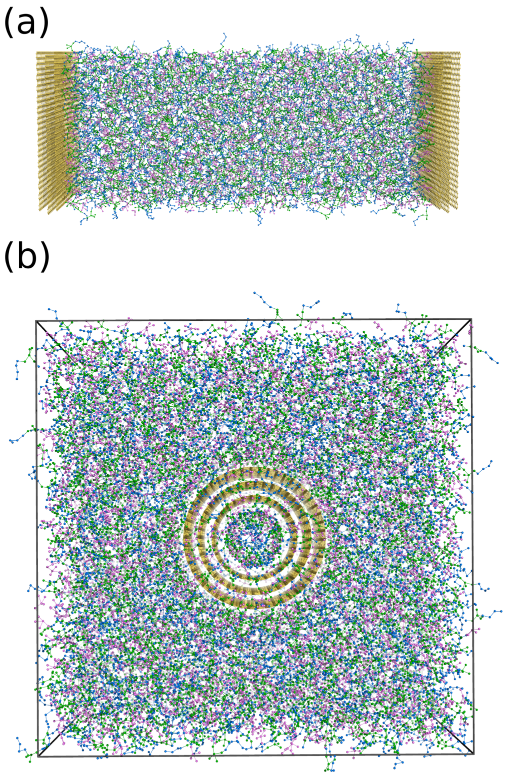

Fig. 2 Snapshots of $[C_4MIM^+][BF_4^-]$ with graphene and CNT. The yellow particles represent carbon atoms, while the colour coding for other beads is the same as in Fig. 1.

immersed in a bulk IL, is depicted in Fig. 2 (b). We adjusted the number of cations and anions to make the whole system electro neutral. The partial charge on each carbon atom is,

$$z_C = -\frac{[N_{C_nMIM^+} - N_{BF_4^-}]}{N_C} \tag{3}$$

where N_C is the number of carbon atoms on the inner layer of CNT. The surface charge density of the inner layer can be calculated as,

$$\sigma_s = \frac{z_C N_C}{2\pi r_C h_C} \tag{4}$$

where r_C and h_C are the radius and the length of the inner layer of the CNT, respectively. The pore size was defined in terms of the diameter of the inner layer, as measured between centres of adjacent carbon atoms. We consider inner pore diameters d, ranging from 0.8 nm to 2 nm systematically. The length of the CNT was fixed at about 6 nm. The LJ parameters of carbon atoms are $\varepsilon_{ww} = 0.36$ kJ/mol and $\sigma_{ww} = 0.34$ nm. The electrode carbon-carbon bond length is fixed at 0.14 nm.[29] All the cross LJ interaction parameters are calculated via the Lorentz-Berthelot mixing rules.

2.3 Molecular dynamics simulation details

All the simulations were performed using the MD simulation software package GROMACS.[30] For the bulk IL systems, 600 pairs of ILs were simulated. In systems containing a cylindrical (electrode) pore, we used about 10000 ion pairs. Such large systems were required in order to ensure bulk-like conditions far away from the pore. Simulations with the flat surface geometry, on the other hand, only required about 1700 ion pairs (adjusted to ensure that the density at the mid-plane between the surfaces, was bulk-like at the relevant temperature). The size of systems containing an explicit cylindrical pore is about $14 \times 14 \times 17$ nm^3. In simulations of planar electrode surfaces, a vacuum part was added in the z direction, such that the periodicity in this dimension was 50 nm. This allows us to use “pseudo-2D” Ewald summations, rather than “proper” 2D Ewald sums.[31]

The simulations for bulk systems were carried out at three different temperatures, 300 K, 400 K and 500 K, in order to check the accuracy of our CG model. Simulations for electrode systems were conducted at 400 K, to avoid the very slow dynamics found at room temperature. We adopted an NPT ensemble for simulations of bulk systems, as well as those containing a cylindrical (electrode) pore. For the planar electrode model, we used an NVT ensemble conditions. The temperature was controlled via a velocity-rescaling thermostat, with a coupling time of 1 ps,[32]. A Berendsen barostat was used for pressure couplings, maintaining the pressure at 1 bar, with a coupling time of 3 ps.[33]

The cut-off radius for LJ interactions and Coulomb interactions in real space was set to 2.0 nm, long ranged electrostatic interactions were solved via the Particle-mesh Ewald (PME) method,[34,35] with a Fourier spacing of 0.3 nm. All the production simulations were carried out for 50 ns, with a 2 fs time step.

3 Bulk properties

In Fig. 3, we show how the bulk density at room temperature changes with cationic alkyl length, n, for $[C_nMIM^+]$, where $n = 2, 4, 6$. In Fig. 4, we show the temperature dependence of the bulk density, for $[C_2MIM^+][BF_4^-]$, $[C_4MIM^+][BF_4^-]$ and $[C_6MIM^+][BF_4^-]$. Predictions from our CG model are compared with corresponding experimental data,[36–40] all-atom simulations with non-polarized force field[41] and polarized force field[42], as well as a previously developed 3-bead CG model.[27]

We see that our CG model of aromatic ILs is able to reproduce experimental bulk density dependencies, on cationic chain length as well as temperature, with a relatively high accuracy.

Switching focus to dynamical properties, a quantity of considerable interest is the self diffusion coefficient, calculated through the Einstein formula:[43]

$$D = \frac{\lim_{t\to\infty} \langle |\mathbf{r}_i(t) - \mathbf{r}_i(0)|^2 \rangle}{2dt} \tag{5}$$

where $\langle |\mathbf{r}_i(t) - \mathbf{r}_i(0)|^2 \rangle$ is the ensemble-averaged mean square displacement (MSD) of the particle, whereas d is the dimension of the space. A linear fit was used to establish the slope.

Simulated diffusion coefficients of cations (c) and anions (a) in $[C_2MIM^+][BF_4^-]$ and $[C_4MIM^+][BF_4^-]$, at three different temperatures, are shown in Fig. 5. Our CG model overestimates the diffusion coefficient for anions under 300 K slightly, but the overall agreement between calculated and experimental diffusion coefficients is quite satisfactory.

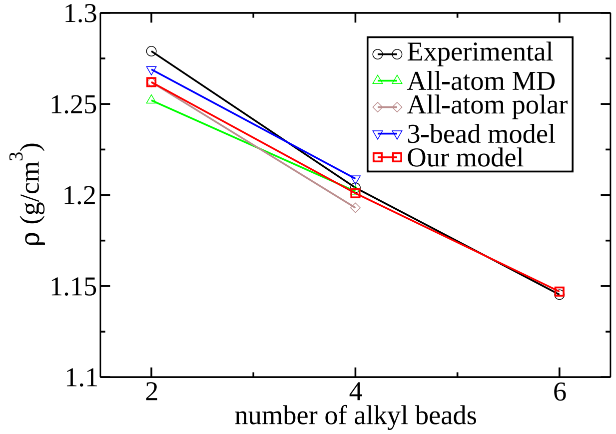

Fig. 3 Simulated bulk densities, utilizing our CG model, as compared with other experimental data,[36,38–40], atomistic simulations[41,42] and 3-bead CG simulations.[27], under different alkyl chain lengths.

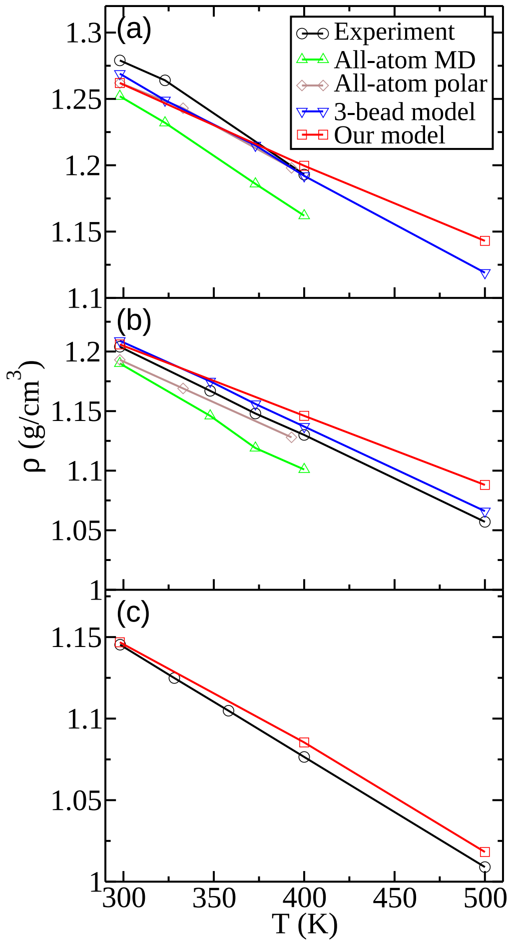

Fig. 4 Bulk densities in our CG model, were compared with other experimental data,[36,38–40a], atomistic simulations[41,42] and 3-bead CG simulations,[27] at various temperatures. (a) [C_2MIM^+][BF_4^-], (b) [C_4MIM^+][BF_4^-], (c) [C_6MIM^+][BF_4^-][b].

[a] *Some of experimental data in higher temperatures were extrapolated via linear fits,*
[b] *there are no other simulation data for [C_6MIM^+][BF_4^-].*

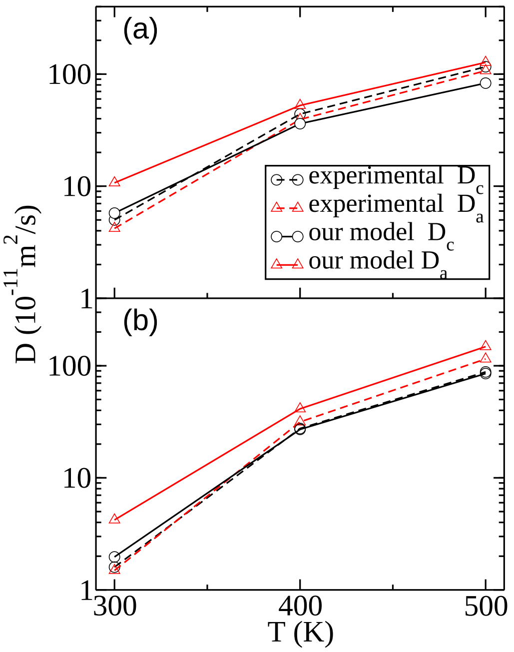

Fig. 5 Predicted diffusion coefficients, as compared with experimental results,[36–38] at various temperatures.
(a) [C_2MIM^+][BF_4^-] (b) [C_4MIM^+][BF_4^-].

Table 1 Shear viscosities of ILs under 400 K and 500 K (units: cP).

[C_2MIM^+][BF_4^-]	400 K	500 K
ours	3.7	1.8
3-bead[27]	5.3	1.8
experiment[36]	4.0	1.7
atomistic[41]	4.0	-
[C_4MIM^+][BF_4^-]	400 K	500 K
ours	4.4	1.4
3-bead[27]	5.1	1.7
experiment[38]	5.4	1.9
atomistic[41]	5.0	-

We have also estimated viscosities of the IL system, using our CG model and the Green-Kubo formula,[44]

$$\eta = \frac{V}{k_{\mathrm{B}}T}\int_0^\infty \langle P_{\alpha\beta}(0)P_{\alpha\beta}(\tau)\rangle \mathrm{d}\tau, \quad \alpha,\beta = x,y,z. \tag{6}$$

where V is the volume of the simulation box, as obtained by a 20 ns average, whereas $P_{\alpha\beta}$ is the off-diagonal component of the pressure tensor.

In Table 1, CG model predictions of viscosities, for [C_2MIM^+][BF_4^-] and [C_4MIM^+][BF_4^-], are compared with corresponding data from other simulations as well as experiments, at 400 K and 500 K. We have not calculated viscosities at room temperature, as they are very high, and it is computationally costly to establish converged data. Still, the agreement with experimental data at the two investigated temperatures, is quite satisfactory.

We believe these comparisons have verified that our CG model for the aromatic imidazolium ILs provides accurate and reliable predictions of static as well as dynamical bulk properties.

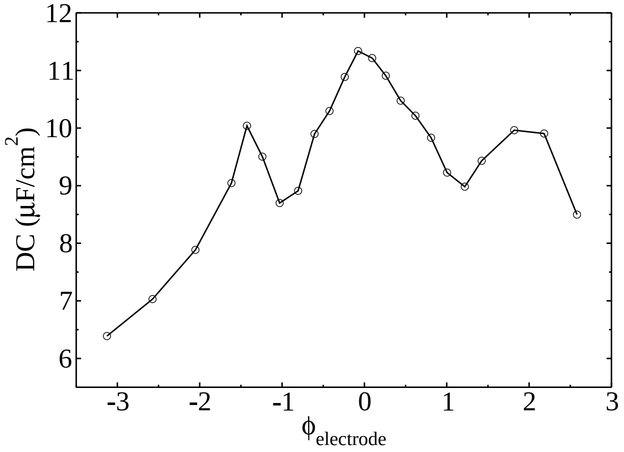

Fig. 6 The DC profiles of graphene slit electrodes.

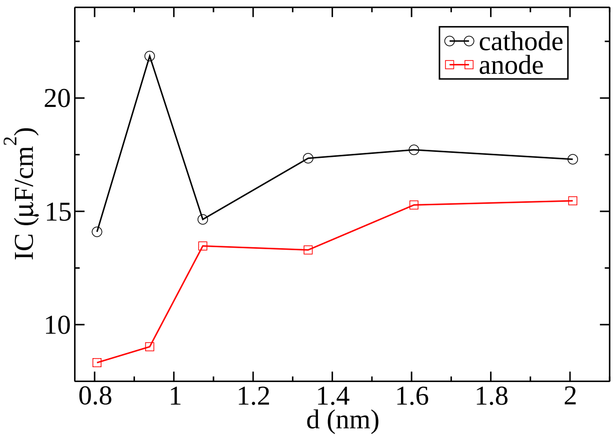

Fig. 7 The integral capacitances in cathode and anode under different CNT pore sizes.

4 Ionic liquids at electrodes

Let us first scrutinize the case of ILs with flat electrode surfaces, as modelled by two widely separated 3-layer graphene surfaces. The electric potential distribution across the slit is then established by the Poisson equation,

$$\phi(z) = -\frac{\sigma_s}{\varepsilon_0 \varepsilon_r} z - \frac{1}{\varepsilon_0 \varepsilon_r} \int_0^z \mathrm{d}z' \int_0^{z'} \rho_e(z'')\mathrm{d}z'' \qquad (7)$$

where z is the perpendicular distance to the graphene surface, while ρ_e is the charge density distribution along the z direction. The potential drop across the EDL layer can be calculated as the potential at the surface minus the potential in the bulk region. The latter is estimated by an average of the potential in the central portion of the slit (near the mid plane).

The integral capacitance (IC) is calculated as the surface charge density divided by the electrode potential,

$$\mathrm{IC} = \frac{\Delta\sigma_s}{\Delta\phi_{\mathrm{electrode}}} \qquad (8)$$

where we choose $\Delta\sigma_s \approx \pm 1$ e/nm^2. The DC is obtained as a derivative:

$$\mathrm{DC} = \frac{\mathrm{d}\sigma_s}{\mathrm{d}\phi_{\mathrm{electrode}}} \qquad (9)$$

The DC is then monitored as a function of electrode potential. Fig. 6 shows the DC profile in the system with flat graphene electrodes. With a flat geometry, the DC curve is somewhat complex, displaying a weak maximum around zero voltage. The DC profile is similar as the simulation work which was done by Hu et al,[45] but the average value is larger than their result (5-6 μF/cm^2). The results from the 3-bead CG model also display close values as Hu et al.[27] Feng and co-workers also provided some results for the same IL in room temperature via atomistic simulation, the capacitances are about 6-8 μF/cm^2, which are between our results and the previous two literatures.[46] But the overall values in our results are close with the experimental works by Alam et al.[47]

The reason that causes the differences might be different force fields of ILs, as well as various parameters for the electrodes. Actually, the capacitances varies under different conditions, for example, temperatures. Lockett and co-workers showed the temperature dependence on capacitance, the capacitance increases with temperature, in additional, the frequencies in impedance methods also influence capacitance sensitively, the capacitance decreases as the frequency increases, the DC profiles also depend on how the potential scanning performs.[48] Breitsprecher et al. studied the ILs based capacitor via CG simulations, they also clarified that the capacitance also depends on the reference point for the potential strongly, since there is a particle-free region between the surfaces and ILs.[49]. We also studied the influence from the particle size of wall (σ_w) on the capacitance recently, which has the similar effect as the distance of the reference points. We found that the capacitance decreases as σ_w increases, which means that we obtained a similar trend.[13]. Thus in a sense, its real value is ambiguous.

As mentioned earlier, we have also simulated the case of a cylinder-shaped pore (CNT) immersed in a bulk IL, i.e. our model of an open pore in a nanoporous electrode. We denote a pore carrying a positive charge densities on the inner surface as a “cathode”, whereas the corresponding negatively charged CNT is denoted as an “anode”. We shall investigate a range of surface charge densities, and cylinder radii.

We have evaluated the electric potential of the CNT by calculating the potential at the inner surface, from all discrete charges in the system, save any possible ones located directly at the position where the potential is measured. As this potential in principle will vary along the inner CNT surface, we calculated the potential, $\phi_{electrode}$, as the average value of sampled potentials at the carbon atoms and at the centre sites of the hexagonal rings formed by connected carbon atoms.[17] In order to avoid edge effects, we have chosen to measure the potential only in the central 2/3 part (along z) of the inner cylinder surface.

The ICs from cathode and anode are shown, for various pore sizes, in Fig. 7. The overall trend, at the anode as well as at the cathode, is that the IC increases slightly with pore size, but the cathode displays a distinct maximum for $d = 0.939$ nm.

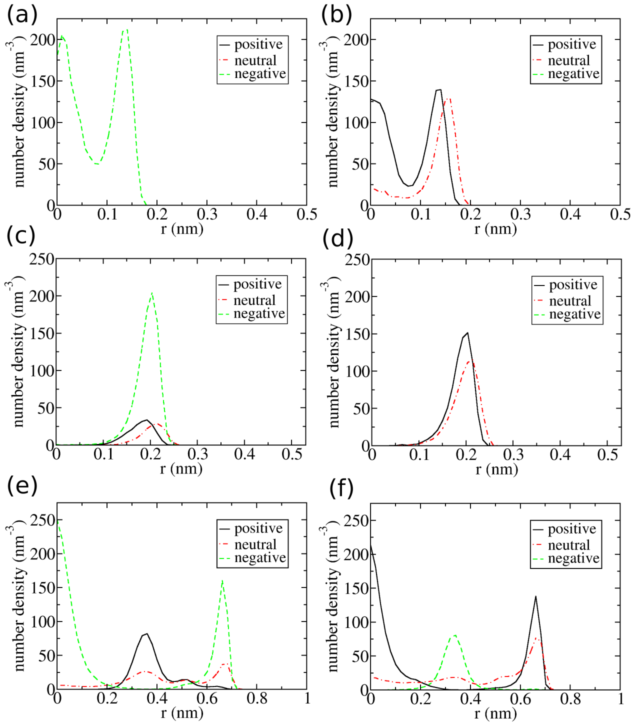

Fig. 8 The number density distributions of CG beads with positive charges, no charges and negative charges versus the distance to the centre axis of the CNTs. (a) $d = 0.939$ nm, σ_s=1.023 e/nm^2, (b) $d = 0.939$ nm, σ_s=-1.023 e/nm^2, (c) $d = 1.073$ nm, σ_s=0.996 e/nm^2, (d) $d = 1.073$ nm, σ_s=-0.996 e/nm^2, (e) $d = 2.007$ nm, σ_s=1.011 e/nm^2, (f) $d = 2.007$ nm, σ_s=-1.011 e/nm^2

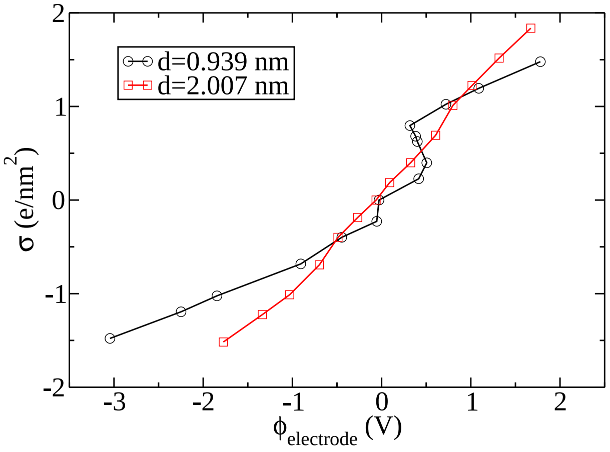

Fig. 9 The relationship between electric potentials and surface charge densities in CNT electrodes.

We shall now try to relate the observed dependence of the integral capacitance on pore size to structural properties of the nanoporous system. Fig. 8 shows the number density distributions of all species of CG beads in the CNT pore. In Fig. 8 (a) and (b), the combination of a high absolute surface charge and a narrow pore size ensures that all coions are expelled from the pore. In those cases, the counterion densities have local maxima at the pore centres as well as at the inner pore surface. These density peaks reflect that the counterions can be found in the CNT pores, and there is a peak in the centre of CNT and another one for charged beads near from the surface in narrow pores, which represents the star architecture of anions and cations, respectively. Thus, there is only one layer of counterions in such a narrow (model of an) electrode pore, i.e. the IL molecules are almost distributed along a straight line in the pore. Note also that the density peaks of anions in a cathode are higher than the corresponding one for cations in an anode. This is presumably related to the smaller volume occupied by an anion, in combination with their polarizablility/volume, as measured by the average LJ strength parameter per bead. Hence, we anticipate a stronger screening, i.e. higher capacitance, at such a narrow cathode pore, than in the corresponding porous anode. One complication is the meaning of "corresponding", since our considerations in principle apply for a certain absolute value of surface charge density, whereas an identical absolute value of the potential might be more relevant in a practical scenario. In wider pores, the relative difference between counterion density peaks in cathodes and anodes is smaller, as shown in Fig. 8. This is obviously related to weaker confinement effects, and for wide pores, we except similar integral capacitances at anodes and cathodes, respectively. We note in graphs (e) and (f) of Fig. 8, that for an inner pore diameter of about 2 nm, the counterion density peaks at the pore surface and at the pore centre, are separated by a coion density peak.

Recall that the cathode IC displays a drop at $d = 1.073$ nm. This is presumably due to the fact that while the pore is wide enough to admit the presence of a significant amount of cations, it is nevertheless too narrow to form a fully established EDL. In other words, cations and anions are forced to pack together in a single layer, the corresponding density distribution is shown in graph (c) of Fig. 8, which reduces the overall electrostatic screening ability of the system. If we continue to increase the pore size, a more "relaxed" EDL layer can be generated in the pore, which leads to an increased IC.

In Fig. 9, we illustrate how the porous electrode surface charge density varies with applied voltage. This is shown for two different pore sizes, $d = 0.939$ nm and $d = 2.007$ nm. We observe (in both cases) an overall increasing trend, reflecting the expected increase of surface charge with applied voltage. However, the narrow pore displays a superimposed oscillation, and this is actually strong enough to generate a non-monotonic dependence. We believe this is related to kinetic (non-equilibrium) effects, and we have in fact verified that one may obtain two distinctly different density distributions, at a surface charge density of 0.5 e/nm^2, depending on the starting conditions "empty" or "filled" pore. Despite running extensive simulations, we have been unable to obtained a converged equilibrium result, in this case. This naturally means that there is some uncertainty regarding the value of the DC at this surface charge density, but it also implies that such narrow pores can generate substantial hysteresis effects at experimental measurements.

We chose the ILs which keep staying inside the CNT pore during the last 20 ns, and calculated the MSDs of the ILs for the entire simulations. Since there is quite a small amount of molecules in the CNT pore, the statistics is not very good, but at least diffusion tendencies can be estimated. Fig. 10 shows the MSDs of the counterions in the CNT pores with $d = 0.939$ nm. Only MSDs of counterions are shown in the figure because there are no coions in the pores with large surface charge densities. Because of the strong confinement, there is virtually no diffusion in x and y dimensions (not shown). The MSDs are roughly flat and sometimes not monotonic, which means that the ILs diffuse much slower than in the bulk system. They are even nearly frozen in some cases, especially at cathodes. This is because there are more anions in the pore, and the effective interactions between ILs and electrodes are stronger due to the smaller volume of anions. The effect of confinement and non-bonded interactions are so strong that the ILs are stuck at the inner surface of the CNT pore. Some experimental and simulation works reported that the ILs have a higher melting point in the CNT pore and stick on the wall of CNT at lower temperatures,[50,51] ILs diffuse much slower if they are close to a graphene surface.[52–54] Hence, some of our results in such a narrow pore depend on the starting conditions "empty" or "filled" pore. Currently we can not make sure that the systems with narrow pores, such as $d = 0.939$ nm have been reached equilibrium after 50 ns simulation. For CNT pores with $d = 2.007$ nm, the ILs are not frozen, although the diffusion is slower than in the bulk systems, with such wide pores do not seem to display equilibrium problems.

In what follows, all results were obtained with an "empty pore" starting configuration. We should thus keep in mind the convergence problems that occur in the system with very narrow pores. At wider pores, we did not find any convergence problems.

The relationship between number densities and surface charge densities are shown in Fig. 11. The number of cations decays rapidly to 0 when the surface charge density $\sigma_s \geq 0.6$ e/nm^2, but the number of anions does not grow rapidly. Hence, the total density drops rather rapidly around this surface charge density.

The DC for a flat surface can be compared with the porous electrode, with $d = 2.007$ nm, in Fig. 12. For the porous electrode, we find the typical "camel-shaped" curve, which was discussed in Sec. 1. With a flat geometry, the DC curve is somewhat more complex, displaying a weak maximum around zero voltage. The overall DC curve for a flat surface is below that for our porous electrode.

5 Conclusions and outlook

A fused CG model for aromatic ILs of type ([$\mathrm{C}_n\mathrm{MIM}^+$][$\mathrm{BF}_4^-$]) has been constructed. The CG model displays excellent transferability for different cationic alkyl chain lengths, and for a range of temperatures. The capacitance of our model IL + porous electrode depends significantly on the pore size, especially in the subnanometre regime. In addition, the relationship between electric potential and surface charge densities is non-monotonic when the pore is narrow. The porous electrode generates an overall enhanced capacitance, as compared with a completely flat electrode.

We are also currently making attempts to construct a classical DFT treatment, based on our coarse-grained ionic liquid model and cylindrical electrode.

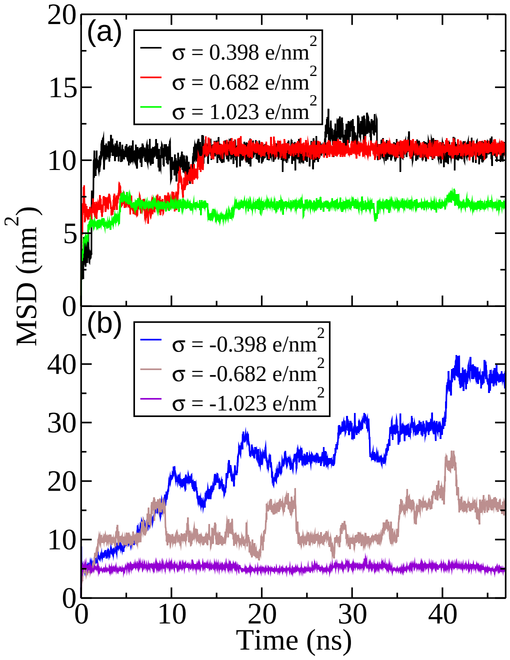

Fig. 10 The MSDs of counterions in the pores with different surface charge densities when $d = 0.939$ nm.

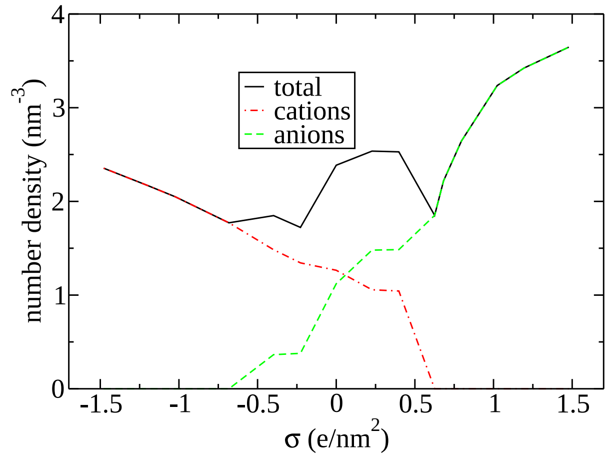

Fig. 11 The relationship between number densities of IL molecules and surface charge densities when $d = 0.939$ nm.

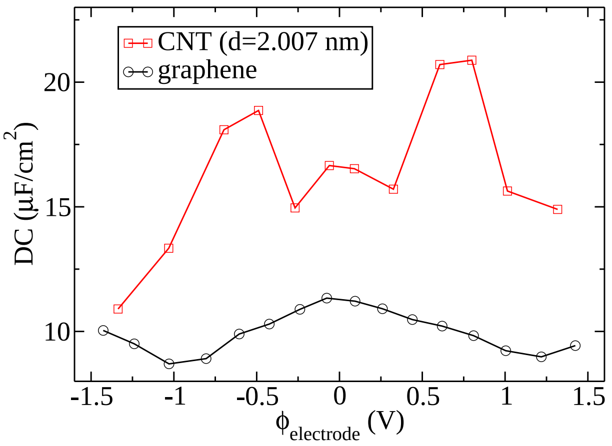

Fig. 12 The DC profiles of CNT electrodes ($d = 2.007$ nm) and graphene slit electrodes, the DC of graphene slit electrodes shows a smaller range than Fig. 6.

6 Acknowledgements

B.L. acknowledges financial support by Carl Tryggers foundation, and J.F. is grateful for the support by the Swedish Research Council. We also appreciate the computing resources, supplied by LUNARC, PDC and UPPMAX.

References

1 N. V. Plechkova and K. R. Seddon, *Chem. Soc. Rev.*, 2008, **37**, 123–150.
2 T. Torimoto, T. Tsuda, K.-i. Okazaki and S. Kuwabata, *Adv. Mater.*, 2010, **22**, 1196–1221.
3 R. P. Swatloski, S. K. Spear, J. D. Holbrey and R. D. Rogers, *J. Am. Chem. Soc.*, 2002, **124**, 4974–4975.
4 H. Liu, K. L. Sale, B. M. Holmes, B. A. Simmons and S. Singh, *J. Phys. Chem. B*, 2010, **114**, 4293–4301.
5 M. V. Fedorov and A. A. Kornyshev, *Chem. Rev.*, 2014, **114**, 2978–3036.
6 M. Armand, F. Endres, D. R. MacFarlane, H. Ohno and B. Scrosati, *Nat. Mater.*, 2009, **8**, 621–629.
7 A. Lewandowski and M. Galiński, *J. Phys. Chem. Solids*, 2004, **65**, 281–286.
8 Y. Chen, X. Zhang, D. Zhang, P. Yu and Y. Ma, *Carbon*, 2011, **49**, 573–580.
9 D. R. MacFarlane, N. Tachikawa, M. Forsyth, J. M. Pringle, P. C. Howlett, G. D. Elliott, J. H. Davis, M. Watanabe, P. Simon and C. A. Angell, *Energy Environ. Sci.*, 2013, **7**, 232–250.
10 A. A. Kornyshev, *J. Phys. Chem. B*, 2007, **111**, 5545–5557.
11 J. Vatamanu, O. Borodin and G. D. Smith, *J. Am. Chem. Soc.*, 2010, **132**, 14825–14833.
12 M. Trulsson, J. Algotsson, J. Forsman and C. E. Woodward, *J. Phys. Chem. Lett.*, 2010, **1**, 1191–1195.
13 J. Forsman, R. Szparaga, S. Nordholm, C. E.Woodward and R. Penfol, *Ionic Liquids - Classes and Properties*, InTech, Rijeka, 2011, pp. 127–150.
14 J. Forsman, C. E. Woodward and M. Trulsson, *J. Phys. Chem. B*, 2011, **115**, 4606–4612.
15 J. Chmiola, G. Yushin, Y. Gogotsi, C. Portet, P. Simon and P. L. Taberna, *Science*, 2006, **313**, 1760–1763.
16 C. Largeot, C. Portet, J. Chmiola, P.-L. Taberna, Y. Gogotsi and P. Simon, *J. Am. Chem. Soc.*, 2008, **130**, 2730–2731.
17 Y. Shim and H. J. Kim, *ACS Nano*, 2010, **4**, 2345–2355.
18 P. Wu, J. Huang, V. Meunier, B. G. Sumpter and R. Qiao, *ACS Nano*, 2011, **5**, 9044–9051.
19 L. Xing, J. Vatamanu, O. Borodin and D. Bedrov, *J. Phys. Chem. Lett.*, 2012, **4**, 132–140.
20 T. A. Centeno, O. Sereda and F. Stoeckli, *Phys. Chem. Chem. Phys.*, 2011, **13**, 12403–12406.
21 Y. Wang, S. Izvekov, T. Yan and G. A. Voth, *J. Phys. Chem. B*, 2006, **110**, 3564–3575.
22 Y. Wang, S. Feng and G. A. Voth, *J. Chem. Theory Comput.*, 2009, **5**, 1091–1098.
23 Y. Ji, R. Shi, Y. Wang and G. Saielli, *J. Phys. Chem. B*, 2013, **117**, 1104–1109.
24 Y.-L. Wang, A. Lyubartsev, Z.-Y. Lu and A. Laaksonen, *Phys. Chem. Chem. Phys.*, 2013, **15**, 7701–7712.
25 D. Sun and J. Zhou, *AIChE J.*, 2013, **59**, 2630–2639.
26 D. Roy and M. Maroncelli, *J. Phys. Chem. B*, 2010, **114**, 12629–12631.
27 C. Merlet, M. Salanne and B. Rotenberg, *J. Phys. Chem. C*, 2012, **116**, 7687–7693.
28 M. Turesson, R. Szparaga, K. Ma, C. E. Woodward and J. Forsman, *Soft Matter*, 2014, **10**, 3229–3237.
29 G. Hummer, J. C. Rasaiah and J. P. Noworyta, *Nature*, 2001, **414**, 188–190.
30 B. Hess, C. Kutzner, D. van der Spoel and E. Lindahl, *J. Chem. Theory Comput.*, 2008, **4**, 435–447.
31 I.-C. Yeh and M. L. Berkowitz, *J. Chem. Phys.*, 1999, **111**, 3155–3162.
32 G. Bussi, D. Donadio and M. Parrinello, *J. Chem. Phys.*, 2007, **126**, 014101.
33 H. J. C. Berendsen, J. P. M. Postma, W. F. van Gunsteren, A. DiNola and J. R. Haak, *J. Chem. Phys.*, 1984, **81**, 3684–3690.
34 T. Darden, D. York and L. Pedersen, *J. Chem. Phys.*, 1993, **98**, 10089–10092.
35 U. Essmann, L. Perera, M. L. Berkowitz, T. Darden, H. Lee and L. G. Pedersen, *J. Chem. Phys.*, 1995, **103**, 8577–8593.
36 A. Noda, K. Hayamizu and M. Watanabe, *J. Phys. Chem. B*, 2001, **105**, 4603–4610.
37 K. Hayamizu, Y. Aihara, H. Nakagawa, T. Nukuda and W. S. Price, *J. Phys. Chem. B*, 2004, **108**, 19527–19532.
38 H. Tokuda, K. Hayamizu, K. Ishii, M. A. B. H. Susan and M. Watanabe, *J. Phys. Chem. B*, 2004, **108**, 16593–16600.
39 C.-L. Wong, A. N. Soriano and M.-H. Li, *Fluid Phase Equilib.*, 2008, **271**, 43–52.
40 A. Muhammad, M. I. Abdul Mutalib, C. D. Wilfred, T. Murugesan and A. Shafeeq, *J. Chem. Thermodyn.*, 2008, **40**, 1433–1438.

41 V. V. Chaban, I. V. Voroshylova and O. N. Kalugin, *Phys. Chem. Chem. Phys.*, 2011, **13**, 7910–7920.

42 O. Borodin, *J. Phys. Chem. B*, 2009, **113**, 11463–11478.

43 M. P. Allen and D. J. Tildesley, *Computer Simulation of Liquids*, Clarendon Press, Oxford, 1987.

44 P. E. Smith and W. F. van Gunsteren, *Chem. Phys. Lett.*, 1993, **215**, 315–318.

45 Z. Hu, J. Vatamanu, O. Borodin and D. Bedrov, *Phys. Chem. Chem. Phys.*, 2013, **15**, 14234–14247.

46 G. Feng, J. Huang, B. G. Sumpter, V. Meunier and R. Qiao, *Phys. Chem. Chem. Phys.*, 2011, **13**, 14723–14734.

47 M. T. Alam, M. M. Islam, T. Okajima and T. Ohsaka, *J. Phys. Chem. C*, 2008, **112**, 16600–16608.

48 V. Lockett, R. Sedev, J. Ralston, M. Horne and T. Rodopoulos, *J. Phys. Chem. C*, 2008, **112**, 7486–7495.

49 K. Breitsprecher, P. Koovan and C. Holm, *J. Phys.: Condens. Matter*, 2014, **26**, 284108.

50 S. Chen, G. Wu, M. Sha and S. Huang, *J. Am. Chem. Soc.*, 2007, **129**, 2416–2417.

51 Y. Jiang, K. Zhang, H. Li, Y. He and X. Song, *Nanoscale*, 2012, **4**, 7063–7069.

52 M. Sha, G. Wu, H. Fang, G. Zhu and Y. Liu, *J. Phys. Chem. C*, 2008, **112**, 18584–18587.

53 M. Sha, G. Wu, Y. Liu, Z. Tang and H. Fang, *J. Phys. Chem. C*, 2009, **113**, 4618–4622.

54 Y.-L. Wang, Z.-Y. Lu and A. Laaksonen, *Phys. Chem. Chem. Phys.*, 2014, **16**, 20731–20740.